Fracture Mechanics of Concrete Structures, de Borst et al (eds) © 2001 Swets & Zeitlinger, Lisse, ISBN 90 2651 825 0

Internal Structure and Fracture in Three Dimensions

Eric N.Landis
University of Maine, Orono, Maine, USA

ABSTRACT: A high resolution three dimensional imaging technique called x-ray microtomography was applied to problems of fracture and damage concrete. The technique can produce images of internal structure, including pores and cracks, at to micron resolution. By applying 3D image analysis techniques we are able to measure crack surface areas, porosity and pore size distribution. Results presented here include applications to damage and fracture in compression, and concrete pore structure.

1. INTRODUCTION

1.1 Background

The heterogeneous nature of concrete produces many interesting experimental and analytical challenges in material and property characterization. Depending on the scale of observation conventional ideas of continuum representations can prove inadequate to capture observed behavior. In fact, the complexity of the material and its sensitivity to ambient conditions, as well as its history, makes it difficult even to draw simple conclusions about behavior.

Although much progress has been made toward an understanding of the various mechanisms involved in the fracture process, there are a number of areas where significant work needs to be done. Among these is a true quantitative relationship between the microstructural features which control fracture behavior and bulk mechanical properties of interest to engineers and designers. The research program described in this paper is an attempt to advance our understanding of the microstructure-property relationship as it applies to damage evolution in portland cement concrete under compressive loading.

1.2 Experimental techniques and analysis

Over the last 40 years, a wide range of experimental techniques have been applied in the study of various microstructure-property relationships in concrete. These techniques include optical and electron microscopy, a range of laser interferrometric techniques, radiographic analysis, ultrasonic and acoustic techniques, conventional stress and strain measurements, and computer vision to name but a few. The challenge here, and the reason we have been using so many different techniques is the fact that with concrete we have a heterogeneous material in which there are heterogeneities over an incredible range of length scales that affect material behavior. Indeed the gel pores that are responsible for creep and shrinkage have dimensions of nanometers, while large aggregates, reinforcements, and cracks that affect strength can have dimensions of meters, depending on the structure. Very few other materials can boast a seven or eight orders of magnitude length scale range.

A traditional trade-off in experimental analysis of concrete is the relationship between range and scale of observation. This is particularly relevant in the digital age where for example a digital image might be fixed at 1024 by 1024 pixels, independent of whether the field of view is 1 micron or 1 meter.

Another trade off has been between observations of surfaces versus internal structure. Historically the trade off has been between high resolution 2D surface imaging and low resolution 3D imaging.

The primary topic of this paper is the use of an experimental technique called x-ray microtomography, which allows us to make high resolution, three dimensional images of internal concrete structure. We may think of microtomography as an experimental technique that compliments our existing array.

2. X-RAY MICROTOMOGRAPHY

X-ray microtomography is a three dimensional radiographic imaging technique. It is similar to conventional x-ray computed tomography (CT) systems used in medical and industrial applications. Unlike those systems, which typically have a maximum spa-

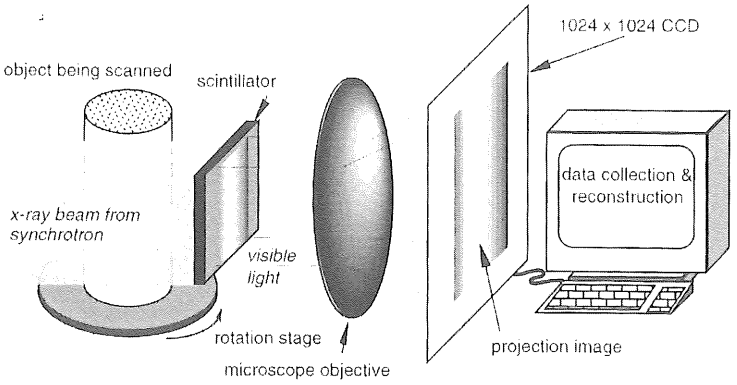

Figure 1. Illustration of experimental setup.

tial resolution of about 1 mm, x-ray microtomography is capable of achieving a spatial resolution close to 1 μm. In both conventional tomography and microtomography, hundreds of 2D projection radiographs are taken of a specimen at different angles. These radiographs are mathematically reconstructed to produce a quantitative three dimensional map of the objects x-ray absorption.(Kak, 1987) Because x-ray absorption is a function of the elemental composition of the object, these x-ray absorption maps can be directly related to the microstructure of the material.

The high resolution of the microtomography system used in this research is the result of using an extremely bright collimated synchrotron x-ray source, and a high resolution scintillator and CCD as the x-ray detector. (Flannery et al, 1987) The facility used in this research resides on beamline X2B at the National Synchrotron Light Source (NSLS) at Brookhaven National Laboratory. Beamline X2B was built by Exxon Research and Engineering specifically for microtomography experiments. A schematic illustration of the facility is shown in Figure 1. As is illustrated in this figure, the specimen sits on a rotation stage so that the it may be viewed from the many different angles required for tomographic reconstruction. The pixel resolution of the system is dictated by the 1024 by 1024 CCD that captures the raw digital images. The CCD used in this work had 24 μm pixels. The viewing area is controlled through the use of a microscope objective lens. A 20X objective produces 1.2 μm pixels for a 1.23 mm field of view, while a 2X objective produces 12 μm pixels for a 12 mm field of view. As discussed above, the high resolution comes at a cost of small specimen size.

The most common way to present tomographic data is in the form of a "slice" image as shown in Figure 2. In these images, brightness is proportional to x-ray absorption. Hence dark regions correspond to low density phases, while light regions correspond to high density phases. The air surrounding the sample, as well as the pore space in the sample appear nearly black. A complete 3D tomographic data set is made up hundreds of these images. Each slice represents the cross section of the object at a different vertical position. Three dimensional renderings of this data may be made by electronically stacking up the slices on top of one another. An example 3D rendering of the Figure 2 data is shown in Figure 3. Note that for qualitative information about the spacial distribution of phases the renderings can be very useful. The 3D data can be sliced and rendered in any arbitrary orientation.

Some previous applications of microtomography in cement and concrete research have produced fruitful results in the study of alkali-silica reaction (Bentz

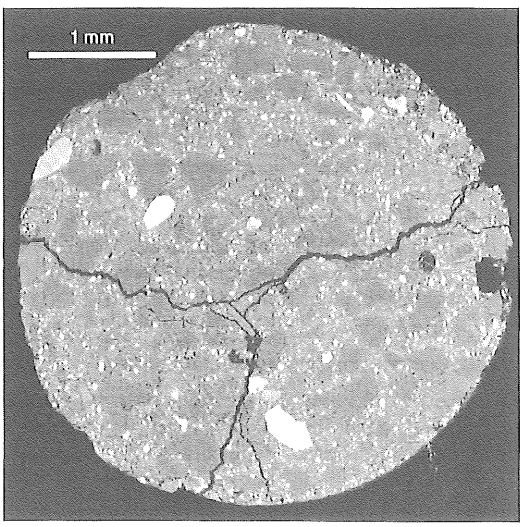

Figure 2. Typical reconstructed microtomographic slice image.

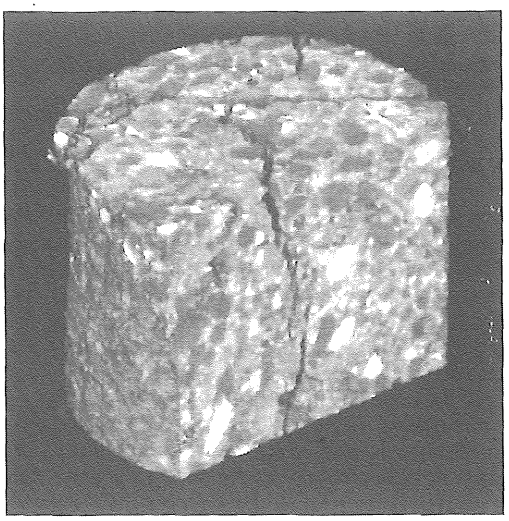

Figure 3. 3D rendering of microtomographic data.

et al, 1995) and encapsulation of hazardous waste materials (Butler et al, 1999). This paper focuses on applications of microtomography towards the study of fracture properties (Landis et al, 1999; Landis and Nagy, 2000) and pore structure (Landis et al, 2000).

3. 3D IMAGE ANALYSIS

While the slice image of Figure 2 and the 3D rendering of Figure 3 are useful for making qualitative observations of internal concrete structure, the real benefit is the quantitative information that can be extracted from the three dimensional data sets. This is because the tomographic data sets represent a 3D map of the material's x-ray absorption profile. The intensity of each image voxel (a voxel is a "volume element" or 3D pixel) is directly proportional to the elemental composition of the material contained in that voxel.

The particular image analysis techniques employed are dictated by the type of information we wish to extract. In this study we were looking at internal cracks and pore space, which may be broadly classified as void space. Therefore we can condense our problem into three steps: first, identify the void space in the images, second, determine the connectivity of that void space, and third, make measurements. Each of these steps is detailed below.

3.1 Image Segmentation

One of the classic problems of digital image analysis is isolating different objects in the image. This is done in a number of ways, but is commonly done through comparison of relative pixel intensity values. For an 8-bit grayscale image such as those produced by the tomographic reconstruction, each pixel (or voxel in the case of 3D analysis) has an intensity value ranging from 0 to 255. In our images 0 is white, while 255 is black. Numbers in between are varying shades of gray. Depending on the objects in the image, one can identify different regions based a comparison with a reference. Pixels of similar intensity can be assumed to belong to a particular object on the image. For example in the images of Figure 2, the blackness surrounding the mortar samples are assumed to be air. This process of reducing an image into its different regions by pixel intensity is known as segmentation, and it is a common image processing technique. (Russ, 1999)

In our case, the segmentation problem is made easier in that we are really only interested in two material phases, air and solid. Our aforementioned problem of identifying the void space is reduced to separating air from solid in the images. Because of this distinction, we can simplify our image analysis by working with binary images. In a binary image, each pixel carries a value of 0 or 1 rather than 0 to 255 as they do in the grayscale images. Thus for our data we segment the image such that dark pixels (air) become 1 and lighter pixels (solids) become 0. An example of a segmented binary image is shown in Figure 4.

3.2 Void connectivity

With a binary image it is easy to distinguish the void space from the solid, so if all we are interested is porosity, we are essentially finished. All we have to do is count the number of black voxels, and divide that count by the total number of voxels in the data

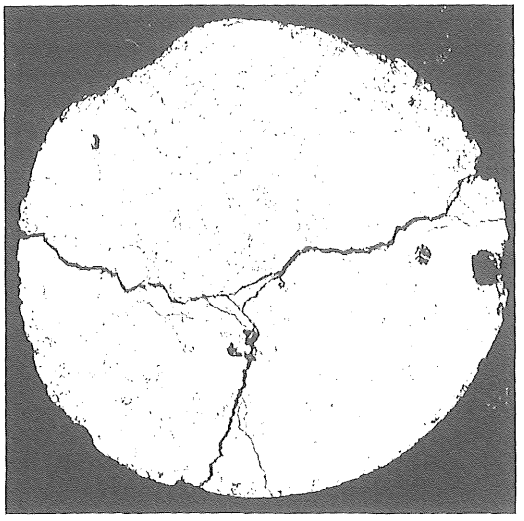

Figure 4. Segmented image of slice of Figure 2.

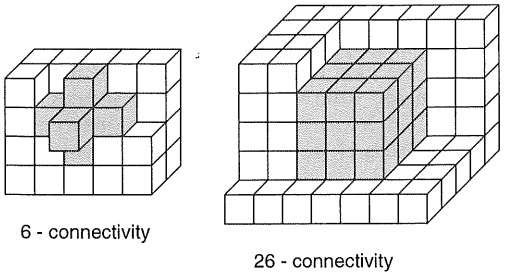

Figure 5. Illustration of voxel connectivity.

set for the fraction of void space. However, if we are interested in the spatial properties of the void space, we need to do a bit more sophisticated analysis. Specifically we need to analyze the connectivity of the black voxels. This is necessary because a large pore will appear in the binary data as a collection of connected black voxels. By analyzing connectivity of black voxels we can identify individual pore spaces and measure their properties.

Note that as shown in Figure 5, one of two possible definitions of connected voxels must be selected. For 6-connectivity, connected voxels must share a face, while for 26-connectivity they may share edges and corners. In this work 26-connectivity was used.

The connectivity analysis procedure works as follows. Starting at the origin of the volume set, the program works its way through the 3D array until it reaches a black voxel. Immediately the voxel is changed to a unique color so it will be identified as a new pore space. Then a connected components procedure is carried out where each of its neighboring 26 voxels is examined. (Note however that only the array indices of greater value need to be checked.) If a neighbor is black, its location is put into a list, if it is not black it is ignored. When the analysis of that voxel is done, the program moves to the next voxel on the list of adjacent voxels, turns it the same color as the initial voxel, and repeats the connected components procedure, looking for adjacent black voxels. Eventually all the black voxels connected to the initial black voxel are found, and labeled with the same color. All voxels adjacent to this object are white, so we may think of the connected voxels as a single isolated pore space. Properties of the pore space can then be measured. In this study, volume and surface area were measured. Volume was determined simply be counting the number of voxels making up the object and multiplying that number by the volume of each voxel. Surface area was determined by counting the number free voxel faces and multiplying that number by the voxel face (pixel) area. Free voxel faces refer to those faces in contact with white voxels. In both measurements we are of course limited by the spatial resolution of the data set.

Once information on void space is determined we are able to relate it to the physical processes of interest such as fracture or permeability as described below.

4. FRACTURE IN COMPRESSION

Fracture mechanics is typically applied in two dimensions. The reason for this is obvious, the analysis is simpler in nearly every aspect. Although we clearly understand that there are out-of-plane phenomena that influence fracture properties, we tend to formulate our analysis in such a way that these effects are captured in a 2D framework.

In the experiments described here, fracture energy was explored in three dimensions. Given the ability to measure internal crack surfaces, we were interested in measuring fracture energy at a most basic level. That is by relating the work required to grow a crack to the resulting change in crack surface area.

A second item of interest was that of fracture energy of a specimen in compression. Fracture of cylinders in compression has traditionally been a difficult problem because of the way that cracks initiate. However, given this method for measuring internal cracking, we have an opportunity to readily observe the processes.

4.1 Experiments

The experiments described here have been detailed in previous papers (Landis and Nagy, 1998; Landis et al, 1999; and Landis and Nagy, 2000).

In order to make microtomographic scans of a specimen under load, a special micro-loading frame was constructed. This frame, shown in Figure 6, was capable of monitoring load and deformation, and it was small enough to fit in the scanning apparatus.

Because of the specimen size limitation we

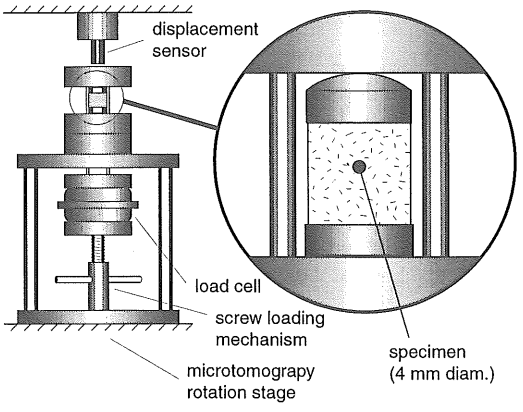

Figure 6. Loading frame for in situ microtomography scanning

focused our attention towards what can be described as the mortar phase of the concrete. At an intermediate scale of observation concrete may be thought of as a two-phase material consisting of aggregates embedded in a mortar matrix. As such, our measurements of fracture energy are not truly valid for what we would typically refer to as "concrete," but rather they will be valid for one phase of that concrete. The specimens were 4 mm diameter by 4 mm high cylinders having a mix proportion of 1 to 2 to 0.6 parts by weight of type I portland cement to sand (.425 mm max. size) to water. The mix was proportioned to correspond roughly to the mortar phase of a conventional normal strength concrete mix. Microtomographic scans were made at a resolution of 6 μm/pixel.

The general procedure was to place a specimen in the loading frame and mount the loading frame on a rotation stage in the x-ray path. An initial tomographic scan was made of the undamaged specimen. A compressive load was then applied to the specimen, and a second scan was taken. After the tomographic scan was completed the specimen was unloaded to measure unloading compliance and reloaded to a higher deformation. As illustrated in Fig. 7, this cycle was repeated several times until the specimen was extensively damaged. Load and displacement data were continuously recorded. A total of six scans were taken during the loading process, including the baseline case.

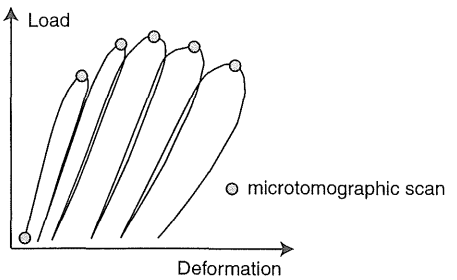

Figure 7. Illustration of loading cycles

4.2 Observations of Internal Damage

The nature of the tomographic data offers some unique perspectives on internal crack growth in materials. Damage, as defined here by microcracks, can be described in different terms.

Figure 8 shows a 1 mm by 1 mm segment of a tomographic slice at four different levels of damage. The corresponding binary images are shown immediately below the grayscale images. The image sequence illustrates the progression of damage in the sample.

It should be noted that three dimensional analysis produces massive amounts of data. For example, the third specimen of Figure 8 (in its entirety) had a total of 758,567 connected objects, or voids. Most of these were only one or two voxels in size. A question arises whether we need to analyze all of these individual voids, or whether we can throw out the smallest as noise. Some of the traditional image processing techniques, such as image subtraction cannot be used because the specimen changes in overall dimensions between scans, so even unchanging void space moves slightly from scan to scan. We

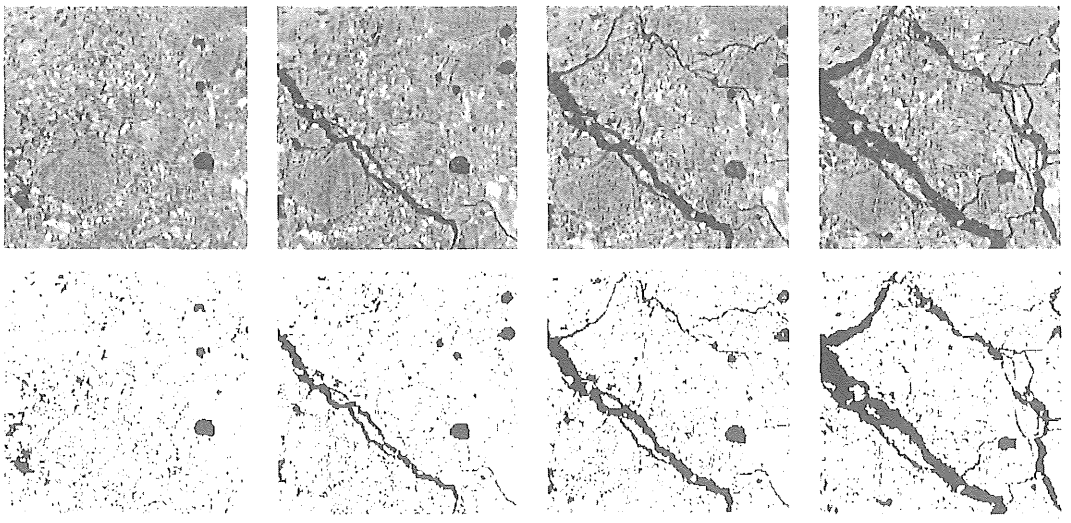

Figure 8. 1 mm square slice at different levels of damage; grayscale and binary images

therefore focused our attention on *changes* from scan to scan.

Table 1. shows some statistics on the connected components, or measured void space and how it changes between scans. The volumes listed are in terms of voxel counts, and areas are in terms of free voxel faces.

We can see that as the load increases, both the volume and the surface area of the void space increase with damage as we would expect. Other observations that can be made from this data are as follows. First, if we look at the largest components, we can see that the ratio of volume to area changes significantly between the first scan and the second scan. if we think of this ratio as a rough shape factor, this indicates that initially the largest void space is made up of shapes that tend to be more spherical. In the second scan we see that surface area grows much faster than volume, hence the formation of a crack that is more planer. This trend does not continue between the third and fourth scan indicating that much of the additional void space in the largest object reflects a widening rather than an extension of an existing crack. If we look at all components, the trend is somewhat different. Surface area grows faster than volume between all scans indicating there is extensive crack growth taking place throughout the specimen.

In the fracture analysis described in the next section, we wish to relate these changes in crack surface area to the external load that causes the damage.

Table 1: Number and size of connected components for specimen at four different levels of damage.

	Totals	>1	>2	>49	Largest
scan 1					
# of CCs	81,604	17,929	6635	624	
volume	448,273			327,431	135,260
area	999,988			364,312	76,457
scan 2					
# of CCs	114,388	26,667	10,023	709	
volume	627,168			453,719	246,115
area	1,531,482			622,262	296,271
scan 3					
# of CCs	157,637	41,056	16,026	833	
volume	784,016			533,933	318,245
area	2,020,725			723,213	373,789
scan 4					
# of CCs	319,854	101,737	46,937	2269	
volume	1,442,456			848,029	501,636
area	4,332,371			1,361,230	556,516

4.3 Fracture Analysis

There are two basic analysis steps required to measure fracture energy from the recorded data. First, for each loading-unloading increment we must calculate the nonrecoverable work-of-load from the recorded load-deformation data. Secondly, we must analyze the tomographic data to measure the incremental change in crack surface area between scans. From these pieces of information, the work-of-fracture can be calculated using the following equation (Broek, 1986):

$$\frac{dW}{dA} = \frac{d}{dA}(F - U) \tag{1}$$

where U is the internal strain energy, F the work of the external load, W the potential energy associated with crack growth, and dA is the incremental change in crack surface area.

It should be noted that there was measurable creep deformation/load relaxation during the 3-4 hours required to complete a tomographic scan. While the distortion in the images is negligible, the error in our work-of-fracture calculation is not. Therefore we modified the work-of-fracture analysis as follows.

For this analysis we assume that creep is an inelastic deformation that is not a function of crack growth. This is entirely reasonable based on the accepted microstructural mechanism of pore water transport (e.g. Mindess and Young, 1981). Then we can define a quantity, C, which is the change in potential energy in the material due to this inelastic deformation. We then add its effect to equation (1) as:

$$\frac{dW}{dA} = \frac{d}{dA}(F - U - C) \tag{2}$$

One additional modification to this relationship is made here because we recognize that our measurements are really made over finite rather than infinitesimal increments. Thus we write equation (2) as:

$$G_{ci} = \frac{\Delta W_i}{\Delta A_i} = \frac{\Delta(F_i - U_i - C_i)}{\Delta A_i} \tag{3}$$

Here G_{ci} is the fracture energy dissipated over loading increment i. F_i, U_i, and C_i are all energy quantities determined directly from the load-deformation data as illustrated in Figure 9. The change in crack surface area, ΔA_i, is determined by taking the difference in total surface area of all connected components between successive tomographic scans. The assumption here is that all changes surface area are due to fracture phenomenon. Undamaged pore space does not change between successive scans.

4.3 Measured Fracture Properties

Figure 10 shows plots of the measurements from two specimens. The cumulative nonrecoverable work-of-load is plotted against the cumulative increase in crack surface area. As shown in the figure, the slope of this plot is the fracture energy G_c. It is interesting to note that the measured values here are comparable

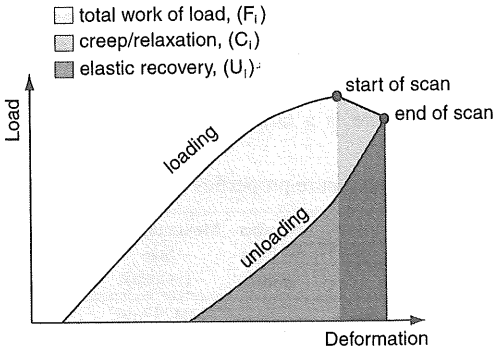

Figure 9. Illustration of terms used in fracture energy calculation.

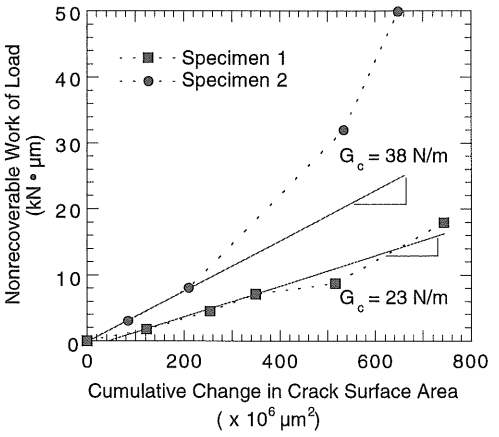

Figure 10. Measured fracture energy in compressior specimens.

to typical measurements of tensile fracture energy, G_f, measured using three point bending. This despite the fact that our loading condition is compression, and we are dealing with a system of cracks as opposed to a single critical crack.

From these plots we see two types of behavior. Specimen 1 shows a moderately constant slope, while specimen 2 shows an increasing work-of-load function of crack area. Both results suggest some interesting behavior.

The case of specimen 2 is fairly straight forward. As concrete has long been referred to as a "quasi-brittle" material that shows toughening behavior, it should exhibit rising R-curve behavior. The increase in slope, and therefore fracture energy could be thought of in terms of rising R-curve behavior.

With specimen 1, however, we have a nearly linear work-crack area relationship. This implies a constant fracture energy for the specimen. That is, equation (3) produces a constant G_c. In this case G_c equals 23 $N \cdot m$ per m^2. Of interest here is whether we can claim the constant G_c shown by specimen 1 is valid for a toughening quasi-brittle material. What we must remember here is that the measurement we are making here is not for a single crack, but rather for a multiple crack system. Because we are dealing with a system of cracks, it can simultaneously be true that a single crack can exhibit rising R-curve behavior, while a system of many cracks shows a more constant work-of-fracture. In fact if we look at only the first few loading increments, both specimens show a relatively constant work-of-fracture as shown in the initial data points of Figure 10. Using the first three data points for specimen 2 we see a constant G_c equal to 38 $N \cdot m$ per m^2. Since we are dealing with short cylinders with no lubrication on the end platens, confinement effects become greater as the specimen deformation becomes larger. The effects of confinement are less in the earlier loading increments shown. Obviously the results presented here are too few to be able to draw any conclusions. However, what these results do show, and perhaps what may summarize the importance of this work, is the fact that when dealing with fracture of concrete in compression we must think in terms of multiple cracks and crack systems.

5. TRANSPORT PROPERTIES

As previously discussed, the nature of the microtomographic data presents us with many opportunities to evaluate various microstructural properties. Because of the importance of concrete durability in long term performance, and because of the relationships between transport properties and durability, we focused attention on how we might use the data to make inferences about the relationships between measurable microstructural properties and permeability. Specifically we were interested if there were any microstructural characteristics that we could relate to permeability.

Towards this end we made microtomographic scans of concrete specimens at various levels of resolution. 3D image analysis of these scans showed several possibilities of ways in which we can relate microstructure to transport properties.

The work described here is based on the analysis of two different data sets. The first was on the same type of 4 mm diameter mortar cylinder that was described in the previous section. The spatial resolution of that data is 6 μm per pixel. The second data set was made of a 1 mm shard that was taken from the remains of a fractured cylinder. The spatial resolution of that data is 1.2 μm per pixel. Slice images from each of those data sets is shown in Figure 11. The combination of the two data sets allows us to look at pore structure in the range from a few millimeters down to a little over a micron.

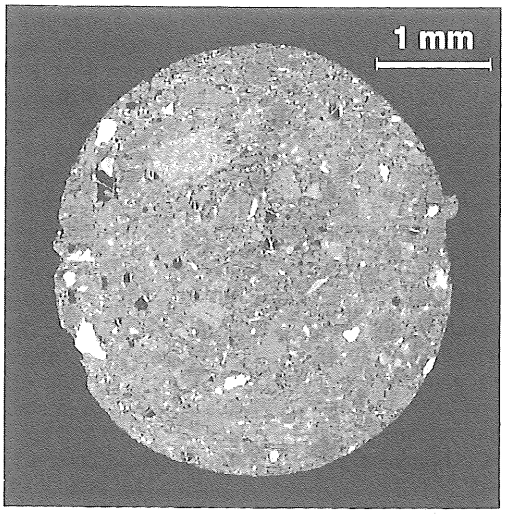

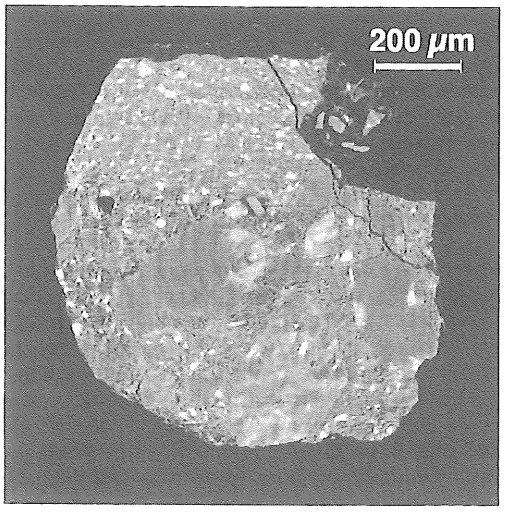

Figure 11. Slice images from the data used for the pore structure analysis.

5.1 Porosity and Pore Size Distribution

Porosity and pore size distribution has traditionally been the key to predicting the long term durability performance of a particular concrete mix. Determination of porosity and pore size distribution in microtomographic images is a relatively straightforward process. Once the images have been segmented to separate void space from solid, porosity is simply the fraction of void space. Data from the pore analysis from these two data sets is presented in Table 2. The porosity for the larger cylinder was 2.64% while the porosity for the shard was 0.96%.

Initially, this porosity result does not seem intuitive. It seems that since we are able to identify smaller pore spaces in the shard specimen, we should be able to observe a greater amount of capillary porosity, as is the case with samples examined using backscattered electron microscopy (Scrivener, 1989). It is possible however, that with the higher magnification scan there is a larger percentage of cement paste. Cement pastes tends to have lower porosities than mortars due to the lack of a high porosity interfacial transition zone (Young, 1987).

Table 2: Measured pore properties

Voxel Size	Sample Volume (voxels)	Number of Pore Spaces	Maximum Pore Size (voxels)	Porosity
6.0 μm	24.4 mm^3 (113,097,334)	495,814	0.0474 mm^3 (219,597)	2.64%
1.2 μm	0.21 mm^3 (126,029,469)	96,479	1.63×10^{-4} mm^3 (94,530)	0.96%

Once all the individual objects (pore spaces) have been identified in the binary image, the determination of pore size distribution is simply a matter of measuring all of the identified objects, and ranking them according to size. In this study pore size was determined by counting the number of voxels in each pore, and by multiplying that count be the voxel volume. (216 μm^3 per voxel for the cylinder, 1.728 μm^3 per voxel for the shard.)

Pore size distributions for both data sets are shown in Figure 12. The distributions are plotted in terms of the cumulative pore fraction as a function of pore volume. It should be noted that the pore sizes range from 1.728 μm^3 to 163,000 μm^3 for the shard, (1.728 μm^3 being the smallest detectable pore volume), and from 216 μm^3 to 47,400,000 μm^3 for the cylinder.

These curves can be compared to some extent with typical mercury intrusion curves (e.g. Cook and Hover, 1993). The difference between this plot and typical intrusion curves is that intrusion curves are typically displayed in terms of equivalent pore diameter as opposed to the pore volume presented here. Herein lies a potential advantage of microtomography as a complementary experimental technique. MIP requires assumptions about pore shapes in order to reach conclusions about pore diameter. With microtomography we have rough spatial information for each individual pore space. Thus, large air-bubble type pore space can be distinguished from flat crack-like space using shape parameters such as surface area to volume ratios. The limitation here being that the closer the pore size is to the minimum detectable, the less reliable that shape information becomes. (All the pore space measured as a single voxel is recorded as a cube).

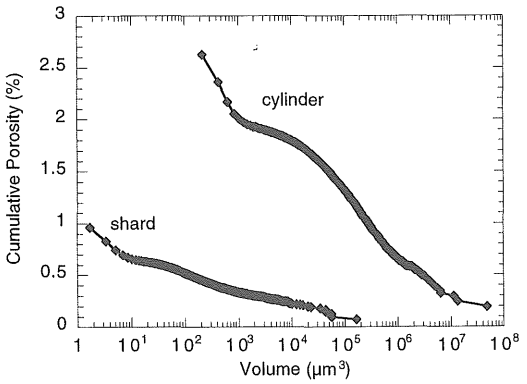

Figure 12. Measured pore size distribution for two data sets.

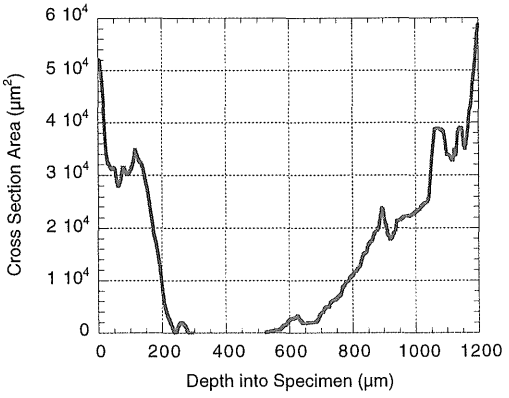

Figure 13. Cumulative pore cross sectional area normal to specimen surfaces.

5.2 Relationships to Permeability

Since the significance of porosity and pore size distribution lies less with their intrinsic relevance, but rather in their relationship with permeability and ultimately durability, we considered how the microtomographic data might be used to examine permeability. Of interest here is the connectivity of the pore spaces to the specimen surface. To analyze this we did a modified connectivity analysis. The modification is that we now consider the outside of the specimen to be part of the pore system, and we wish to track the amount of pore space inside the specimen that is connected to the surface. This surface connectivity measurement relates to how easily fluid can permeate into the material.

The specific procedure used here was to start with a cube 1.2 mm (200 pixels) on each side, extracted from the cylinder data. The cube was segmented to separate air from solid as described above. The top and bottom most slices were used to define the outside of the specimen, and all voxels in those planes were set to an arbitrary color (say red). Then a connected components routine was run slice by slice so that every air black air voxel that was connected to a red voxel was changed to red. At the end of this routine, each slice consisted pixels of three possible colors: white for solid, red for air connected to the top or bottom surface, and black for air not connected to the surface. The total area of the pore space connected to the surface (all red pixels) was measured for each slice. This measurement is shown in Figure 13. This figure shows the sum of all pore areas as a function of depth into the specimen. The fact that the plot goes to zero at the center indicates that there exists a segment of the cube that is inaccessible from the exterior through a pore network greater that 6 μm. It should be noted that pore cross section area is defined as the area in a plane parallel to the top and bottom surface planes.

Obviously the greater the inaccessible volume, or in this case the larger amount of depths where a plot such as Figure 13 is zero, the greater the likelihood we have a relatively impermeable concrete. Current work in progress is aimed at quantifying permeability for given microstructures.

The interesting thing to note about the plot of Figure 13 is how the connected pore area constricts with depth, as we might expect. However it periodically opens up. If one were to model the flow of water through though this pore system, the effect of opening and closing pore networks would need to be considered.

6. SUMMARY AND CONCLUSIONS

The work described in this paper is aimed at better quantifying microstructure-property relationships for cement-based materials. X-ray microtomography is a powerful tool for examining these relationships as it allows us to observe internal structure at relatively high spatial resolution. Using 3D image analysis techniques we are able to make quantitative analyses of microstructure, and the changes that occur as a result of damage and fracture.

Some observations that have been made through research to date:

- We have shown that using an experimental setup where tomographic scans are made of a specimen under load, changes in internal damage can measured using three dimensional image analysis techniques.
- When load and deformation data are available, we can make a work of fracture calculation based on the tortuous crack surfaces that arise in the fracture of heterogeneous materials.
- For small mortar specimens loaded in compression, we can have a relatively constant work of

fracture if we consider the total area of all the crack systems involved.

- We can measure pore size distributions to a resolution approaching 1 μm. The advantage here is that no assumptions about pore shape are required.
- We can examine pore connectivity in relationship to the surface of the material, and can track the path of least resistance that deleterious agents will take to the interior of the specimen.

Current and future work is aimed at relating the three dimensional data obtained to computational models for both mechanical properties, and multiphase flow and transport.

7. ACKNOWLEDGEMENTS

This work is supported by the U.S. National Science Foundation (CMS-9733769) under a program directed by Dr.Vijay Gopu. Parts of this research was conducted at the National Synchrotron Light Source, Brookhaven National Laboratory, which is supported by the U.S. Department of Energy, Division of Materials Sciences and Division of Chemical Sciences (DOE contract number DE-AC02-76CH00016.)

8. REFERENCES

Bentz, D. P., Martys, N. S., Stutzman, P. E., Levenson, M. S., Garboczi, E. J., Dunsmuir, J., and Schwartz, L. M. (1995). "X-Ray Microtomography of an ASTM C109 Mortar Exposed to Sulfate Attack." Microstructure of Cement-Based Systems/Bonding and Interfaces in Cementitious Materials, S. Diamond et al., eds., Pittsburgh, 77-82.

Broek, D. (1986). Elementary Engineering Fracture Mechanics, 4th Edition. Boston, Martinus Nijhoff Publishers, Dordrecht.

Butler, L. G., Cartledge, F. K., Owens, J. W., and Dowd, B. "Synchrotron X-ray Microtomography and Solid-State NMR of Environmental Wastes in Cement." Developments in X-Ray Tomography II, SPIE 3772, Denver, 97-104.

Cook, R. A., and Hover, K. C. (1993). "Mercury Porosimetry of Cement-Based Materials and Associated Correction Factors." ACI Materials Journal, 90(2), 152-161.

Deckman, H. W., Dunsmuir, J. H., D'Amico, K. L., Ferguson, S. R., and Flannery, B. P. (1991). "Development of Quantitative X-ray Microtomography." Materials Research Society Symposium Proceedings, 217, 97-110.

Flannery, B. P., Deckman, H. W., Roberge, W. G., and D'Amico, K. L. (1987). "Three-Dimensional X-ray Microtomography." Science, 237, 1439-1444.

Kak, A. C., and Slaney, M. (1987). Principles of Computerized Tomographic Imaging, IEEE Press.

Landis, E. N., and Nagy, E. N. "Work of Load Versus Internal Crack Growth for Mortar in Compression." Third International Conference on Fracture Mechanics of Concrete Structures, Gifu, 35-46.

Landis, E. N., Nagy, E. N., Keane, D. T., and Nagy, G. (1999). "A Technique to Measure Three-Dimensional Work-of-Fracture of Concrete in Compression." Journal of Engineering Mechanics, 125(6), 599-605.

Landis, E. N., and Nagy, E. N. (2000). "Three-dimensional Work of Fracture for Mortar in Compression." Engineering Fracture Mechanics, 65(2), 223-234.

Landis, E. N., Petrell, A. L., Lu, S., and Nagy, E. N. (2000). "Examination of Pore Structure Using Three Dimensional Image Analysis of Microtomographic Data." Concrete Science and Engineering, 2(8), 162-169.

Mindess, S., and Young, J. F. (1981), Concrete, Prentice-Hall Inc. Englewood Cliffs, NJ.

Russ, J. C. (1999). The Image Processing Handbook, CRC Press/IEEE Press, Boca Raton.

Scrivener, K. L. (1989). "The Use of Backscattered Electron Microscopy and Image Analysis to Study the Porosity of Cement Paste." Pore Structure and Permeability of Cementitious Materials, L. R. Roberts and J. P. Skalny, eds., MRS, 129-140.

Young, J. F. (1987). "A Review of the Pore Structure of Cement Paste and Concrete and its Influence on Permeability," in Permeability of Concrete, ACI SP-108, 1-8.